

Supplemental Material for “Bicircular Light Floquet Engineering of Magnetic Symmetry and Topolgy and Its Application to the Dirac Semimetal Cd₃As₂”

Thaís V. Trevisan,^{1,2,*} Pablo Villar Arribi,³ Olle Heinonen,³ Robert-Jan Slager,^{4,5} and Peter P. Orth^{1,2,†}

¹*Ames Laboratory, Ames, Iowa 50011, USA*

²*Department of Physics and Astronomy, Iowa State University, Ames, Iowa 50011, USA*

³*Materials Science Division, Argonne National Laboratory, Lemont, Illinois 60439, USA*

⁴*TCM Group, Cavendish Laboratory, University of Cambridge, Cambridge CB3 0HE, United Kingdom*

⁵*Department of Physics, Harvard University, Cambridge MA 02138, USA*

(Dated: January 24, 2022)

CONTENTS

A. BCL setup	1
B. k.p model for cadmium arsenide	2
1. Semimetallic phase	3
2. Insulating phase	4
C. Light-induced mass terms	5
D. Controlling the position of the Weyl nodes	7
E. Higher-order terms in the effective Hamiltonian	7
F. Validity of the high-frequency expansion	8
G. Surface states	9
H. Temperature dependence of the GME effect	11
References	12

Appendix A: BCL setup

The polarization state of the BCL field,

$$\mathbf{A}(t) = \mathcal{A}_0 \sqrt{2} \operatorname{Re} \left[e^{-i(\eta\omega t - \alpha)} \boldsymbol{\varepsilon}_R + e^{-i\omega t} \boldsymbol{\varepsilon}_L \right] \quad (\text{A1})$$

is specified by its incidence direction \hat{q} , frequency ratio η between the two combined CL and their phase difference α . The dependence on \hat{q} is encoded in the vectors $\boldsymbol{\varepsilon}_R$ and $\boldsymbol{\varepsilon}_L$ that span the light polarization plane. Here, we make this dependence more explicit.

We choose \hat{x} , \hat{y} and \hat{z} to coincide with the Cd₃As₂ crystallographic axes $\hat{a} \equiv [100]$, $\hat{b} \equiv [010]$ and $\hat{c} = [001]$. A BCL is then incident with an angle φ with respect to the normal of the (001) surface of the material, i.e. the surface perpendicular to \hat{z} , as illustrated in Fig. 1(a). In this case, the incidence direction is simply $\hat{q}_0 = (0, \sin \varphi, -\cos \varphi)$, which is the same incidence direction of the CLs combined in the BCL wave. The polarization plane is spanned by the vectors $\hat{\varepsilon}_{0,1}$ and $\hat{\varepsilon}_{0,2}$. We set $\hat{\varepsilon}_{0,1} = \hat{x} = (1, 0, 0)$, and $\hat{\varepsilon}_{0,2} = (0, -\cos \varphi, -\sin \varphi)$ is obtained by rotating $\hat{\varepsilon}_{0,1}$ by $\pi/2$ around \hat{q}_0 in order to satisfy $\hat{\varepsilon}_{0,1} \times \hat{\varepsilon}_{0,2} = \hat{q}_0$ (see Fig. 1(b)).

* thais@iastate.edu

† porth@iastate.edu

A more generic incidence direction can be straightforwardly constructed from this simple case by rotating the incident plane by an angle β around \hat{z} , as illustrated in Fig. 1(c). In this case, we have

$$\hat{q} = R_{\hat{z}}(\beta)(0, \sin \varphi, -\cos \varphi) = (-\sin \beta \sin \varphi, \cos \beta \sin \varphi, -\cos \varphi) . \quad (\text{A2})$$

$$\hat{\varepsilon}_1 = R_z(\beta)(1, 0, 0) = (\cos \beta, \sin \beta, 0) , \quad (\text{A3})$$

$$\hat{\varepsilon}_2 = R_z(\beta)(0, -\cos \varphi, -\sin \varphi) = (\cos \varphi \sin \beta, -\cos \varphi \cos \beta, -\sin \varphi) . \quad (\text{A4})$$

For a light circularly polarized to the right, the polarization is specified by $\varepsilon_R = (\hat{\varepsilon}_1 - i\hat{\varepsilon}_2)/\sqrt{2}$, while the polarization state of a light circularly polarized to the left is given by $\varepsilon_L = (\hat{\varepsilon}_1 + i\hat{\varepsilon}_2)/\sqrt{2}$. Substituting ε_R and ε_L into Eq. (A1), we can write the Cartesian components of the BCL vector potential in a compact form:

$$A_\mu(t) = \mathcal{A}_0 c_\mu [\cos(\eta\omega t - \alpha) + \cos(\omega t)] + \mathcal{A}_0 d_\mu [\sin(\eta\omega t - \alpha) - \sin(\omega t)] , \quad (\text{A5})$$

where $\mu = x, y, z$. The coefficients c_μ and d_μ are parametrized by the two angles φ and β , as shown in Table A.

Note that a BCL perpendicular to (001) or, equivalently, parallel to $\hat{z} = [001]$ is obtained by setting $\beta = 0$ and $\varphi = \pi$. Since Cd_3As_2 is a tetragonal crystal, the correspondence between the indices for the surface (hkl) and its normal $[uvw]$ follows [1]

$$\frac{u}{h} = \frac{v}{k} = \frac{w}{l} \left(\frac{c}{a} \right)^2 , \quad (\text{A6})$$

where $a = b$ and c are the lattice parameters in the xy plane and in \hat{z} direction, respectively. For Cd_3As_2 , $a = 12.633\text{\AA}$ and $c = 25.427\text{\AA}$ [2], but for calculations purposes we set $c = 2a$. In this case, a BCL normal to (112) is parallel to the $[221] = \hat{x} + \hat{y} + \hat{z}$ direction and, therefore, obtained by setting $\beta = -\pi/4$ and $\varphi = \arccos(-1/\sqrt{3})$.

Appendix B: k.p model for cadmium arsenide

In this appendix, we specify the form of the momentum-dependent coefficients of the k.p model shown in Eq.(2) in the main text for Cd_3As_2 . We discuss both semimetallic and insulator states.

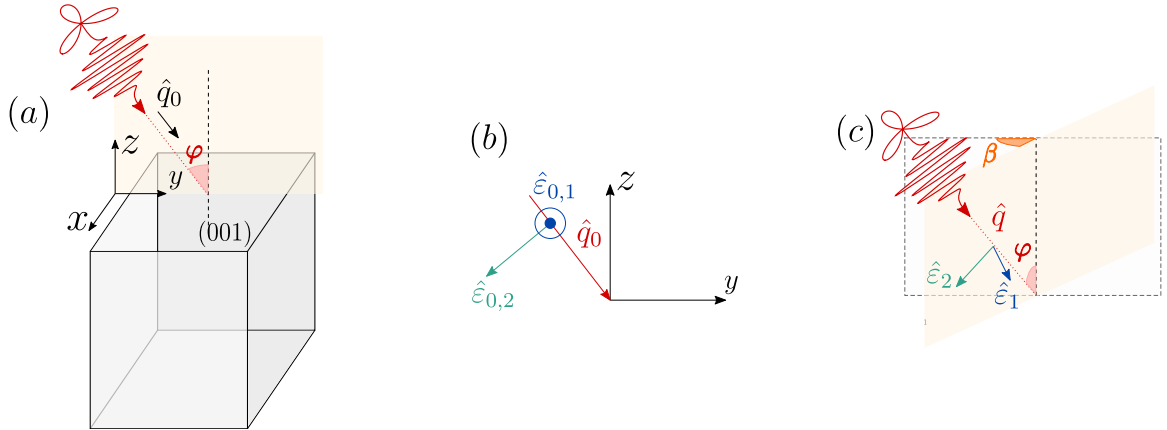


FIG. 1. (a) Illustration of the tetragonal Cd_3As_2 crystal irradiated by a BCL incident with an angle φ with respect to the normal of the (001) surface. (b) Light propagation direction \hat{q}_0 and vectors ε_1 and ε_2 defining the polarization plane for the setup shown in (a). Incidence direction and polarization vectors for a generic incidence direction.

	x	y	z
c_μ	$\cos \beta$	$\sin \beta$	0
d_μ	$-\sin \beta \cos \varphi$	$\cos \beta \cos \varphi$	$\sin \varphi$

TABLE I. Coefficients of the Cartesian components of the BCL field.

1. Semimetallic phase

Despite its complicated crystal structure, first-principle calculations show that the low energy physics of Cd_3As_2 is characterized by a minimal 4-band model [3],

$$\hat{H} = \sum_{\mathbf{k}} \hat{\psi}_{\mathbf{k}}^\dagger \hat{h}(\mathbf{k}) \hat{\psi}_{\mathbf{k}}, \quad (\text{B1})$$

$$\hat{h}(\mathbf{k}) = M_{\mathbf{k}}\sigma_0\tau_z + P_{\mathbf{k}}\sigma_z\tau_x - Q_{\mathbf{k}}\sigma_0\tau_y + \varepsilon_{\mathbf{k}}\sigma_0\tau_0. \quad (\text{B2})$$

This model is a down-fold from an 8×8 Hamiltonian spanning the basis of Cs $5s$ and As $4p$ states where spin-orbit coupling is already accounted for locally. This Hamiltonian is diagonalized into the J basis and then a downfolded to 4-band model spanning the following basis set $\{|S_{1/2}, 1/2\rangle, |P_{3/2}, 3/2\rangle, |S_{1/2}, -1/2\rangle, |P_{3/2}, -3/2\rangle\}$. Due to the further symmetry breaks of the problem (e.g. tetragonal-orthorhombic due to strain and spatial inversion), new off-diagonal terms are included in the 4 effective Hamiltonian that mix the different states in this reduced basis set, but these off-diagonal terms are added after the diagonalization into the J -basis, leading to Eq.(B2). All these terms accounting for the different symmetry breaks in this 4-band low-energy effective model have been previously introduced by Ref. 3 and the model itself has been already used to describe surface states in Cd_3As_2 [3–5]. In Eq.(B2), $\hat{\psi}_{\mathbf{k}}^\dagger \equiv (c_{\mathbf{k},\uparrow}^\dagger, d_{\mathbf{k},\uparrow}^\dagger, c_{\mathbf{k},\downarrow}^\dagger, d_{\mathbf{k},\downarrow}^\dagger)$, where $c_{\mathbf{k},\sigma}^\dagger$ ($d_{\mathbf{k},\sigma}^\dagger$) creates an electron with momentum \mathbf{k} and spin σ in the $5s$ ($4p$) orbital Cd (As). Besides, σ_j (τ_j), with $j = x, y, z$ are Pauli matrices in spin (orbital) space and σ_0 and τ_0 are two-by-two identity matrices. The functions preceding the Pauli matrices in Eq. (B2) are polynomials of the momentum components,

$$M_{\mathbf{k}} = M_0 - M_1 k_z^2 - M_2 (k_x^2 + k_y^2), \quad (\text{B3})$$

$$P_{\mathbf{k}} = A k_x, \quad (\text{B4})$$

$$Q_{\mathbf{k}} = A k_y, \quad (\text{B5})$$

$$\varepsilon_{\mathbf{k}} = C_0 + C_1 k_z^2 + C_2 (k_x^2 + k_y^2). \quad (\text{B6})$$

with coefficients calculated in Ref. [4] and summarized in Table II. Such a simple $k.p$ model is able to capture the two Dirac cones in the band structure of Cd_3As_2 because they occur in the vicinity of the Γ point ($\mathbf{k} = 0$) of the Brillouin zone, as shown in Fig. 2. The separation between the valence and conduction band at the center of the Brillouin zone gives the the Lifshitz energy $E_{Lif} = 60$ meV. The Lifshitz energy corresponds to the energy scale over which the shape of the Fermi surface changes from a single pocket to two separate pockets and later back to a single pocket.

It is important to note that terms such as Eqs. (B4) and (B5) originate from $\sin(ak_x)$ and $\sin(ak_y)$, respectively, in the tight-binding model valid in the entire Brillouin zone expanded to linear order in momentum. We noticed, however, that when light is coupled to the electrons, we need to carry the expansion at least up to third order in momentum for the symmetries of the Floquet Hamiltonian to be consistent with those preserved by the light vector potential. Accordingly, we add corrections γk_x^3 and γk_y^3 to Eq. (B4) and Eq. (B5), respectively. Symmetry allows for the coefficients of the linear and cubic terms in Eq. (B4) and Eq. (B5) to be different, and we choose $\gamma = A/6$ to ensure that the new cubic terms are only a small correction to the original expressions. Similarly, for linear terms in k_z that will appear later in the presence of strain, we add a correction four times larger ($4\gamma k_z$, with $\gamma = B_1/6$ - see Eq. (B8)) to reflect $c = 2a$.

Parameters	Semimetallic	Insulating
M_0 (eV)	0.0282	0.0374
M_1 (eV \AA^2)	20.72	20.36
M_2 (eV \AA^2)	13.32	18.77
C_0 (eV)	-0.0475	0.0113
C_1 (eV \AA^2)	12.50	12.05
C_2 (eV \AA^2)	13.62	13.13
A (eV \AA)	1.116	1.089
B_1 (eV \AA)	0	0.2566

TABLE II. Parameters for the $k.p$ model for Cd_3As_2 in both semimetallic (Dirac semimetal) and insulating (strong TI) phases. Values taken from Ref. [4]. Note that in Ref. [4] M_1 and M_2 are defined with a global minus sign. Here, we incorporated it directly in Eqs. (B3) and that is why M_1 and M_2 are positive in our table.

2. Insulating phase

The effects of strain in the plane perpendicular to \hat{z} are incorporated in the $k.p$ model by adding extra terms to Eq. (B2) that break the desired symmetries. The values of the coefficient in the polynomial functions changes (see Table II), and so does the Lifshitz energy, which becomes $E_{Lif} = 80$ meV. The form of the symmetry-breaking terms depend on the type of strain we consider.

Let's start with strain type B_{1g} introduced in Ref. 4. It breaks the two-fold rotations around the diagonals in the xy plane $C_{2,[110]}$ and $C_{2,[1\bar{1}0]}$ (and the corresponding mirrors $M_{[110]}$ and $M_{[1\bar{1}0]}$) in addition to C_{4z} . All other symmetries of the unstained material remain unchanged and, as a consequence, Cd_3As_2 with B_{1g} strain is characterized by the space group $Pcca$ (No. 54). Time-reversal is also preserved in the absence of light and the corresponding magnetic space group is the grey group $Pcca1'$ (No.54.337). The generic first-quantized Hamiltonian that preserves the symmetries of this group is given by

$$\hat{h}_{B_{1g}}(\mathbf{k}) = M_{\mathbf{k}}\sigma_0\tau_z + B_{\mathbf{k}}\sigma_x\tau_x + P_{\mathbf{k}}\sigma_z\tau_x - Q_{\mathbf{k}}\sigma_0\tau_y + \varepsilon_{\mathbf{k}}\sigma_0\tau_0, \quad (\text{B7})$$

with [4]

$$B_{\mathbf{k}} = B_1 \left(k_z + \frac{2k_z^3}{3} \right). \quad (\text{B8})$$

The functions $M_{\mathbf{k}}$, $P_{\mathbf{k}}$, $Q_{\mathbf{k}}$ and $\varepsilon_{\mathbf{k}}$ have the same form as in the semimetallic case, but with different coefficients (see Table II).

Strain of type B_{2g} in the xy plane, on the other hand, breaks, besides C_{4z} , the two-fold rotations around the crystallographic axes $C_{2,x}$ and $C_{2,y}$, as well as their corresponding mirrors, but preserves $C_{2,[110]}$ and $C_{2,[1\bar{1}0]}$. The resulting space group is $Fddd$ (No. 70). The first-quantized $k.p$ Hamiltonian with all the terms allowed by the symmetries of this group was obtained using python Qsymm [6] and reads

$$\hat{h}_{B_{2g}}(\mathbf{k}) = \tilde{M}_{\mathbf{k}}\sigma_0\tau_z + B_{\mathbf{k}}\sigma_y\tau_x + \tilde{P}_{\mathbf{k}}\sigma_z\tau_x - \tilde{Q}_{\mathbf{k}}\sigma_0\tau_y + \tilde{\varepsilon}_{\mathbf{k}}\sigma_0\tau_0, \quad (\text{B9})$$

where

$$\tilde{M}_{\mathbf{k}} = M_{\mathbf{k}} + s_A k_x k_y, \quad (\text{B10})$$

$$\tilde{P}_{\mathbf{k}} = P_{\mathbf{k}} + \tilde{A} k_y \left(1 + \frac{k_y^2}{6} \right), \quad (\text{B11})$$

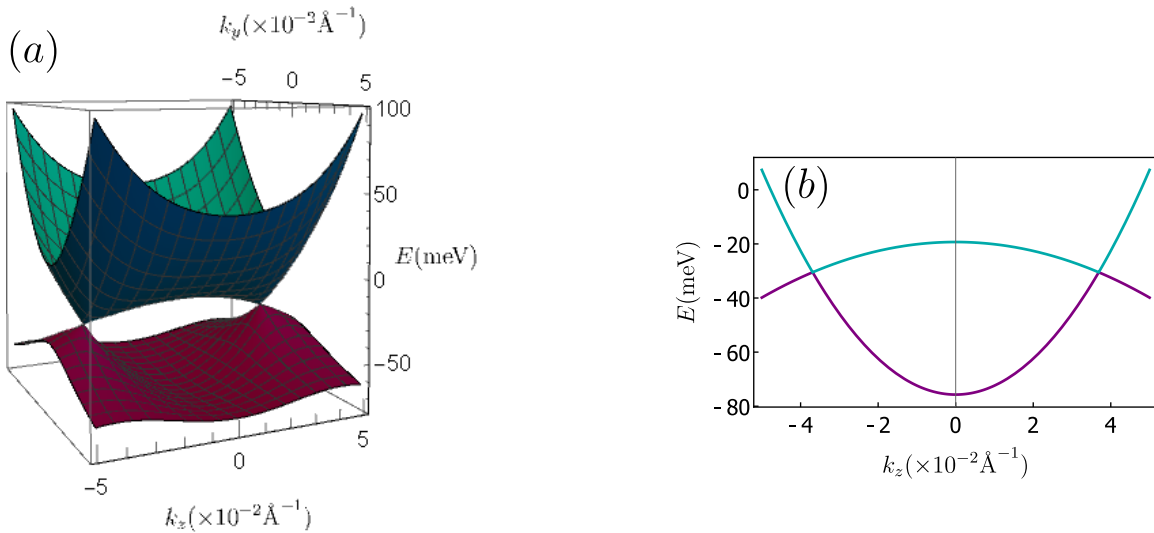


FIG. 2. Bulk bands of the $k.p$ model for Cd_3As_2 in the absence of strain and light [Eq.(B2)]. We set (a) $k_x = 0$ and (b) $k_x = k_y = 0$.

$$\tilde{Q}_{\mathbf{k}} = Q_{\mathbf{k}} + \tilde{A}k_x \left(1 + \frac{k_y}{6}\right), \quad (\text{B12})$$

$$\tilde{\varepsilon}_{\mathbf{k}} = \varepsilon_{\mathbf{k}} + s_B k_x k_y, \quad (\text{B13})$$

and $M(\mathbf{k})$, $P(\mathbf{k})$, $Q(\mathbf{k})$, $\varepsilon(\mathbf{k})$ and $B(\mathbf{k})$ defined in Eqs. (B3)-(B6) and Eq. (B8), respectively. For simplicity, we set, for simplicity, $s_A = s_B = \tilde{A} = B_1 = 0.2566 \text{ eV}\text{\AA}$.

Appendix C: Light-induced mass terms

Here, we show the expressions for the light-induced mass terms $\hat{m}(\mathbf{k})$ defined in the main text. Standard high-frequency expansion [7–10] tell us that a time-independent effective Hamiltonian \hat{H}_{eff} can be derived from a generic periodic Hamiltonian $\hat{H}(t) = \hat{H}(t + T)$ using

$$\hat{H}_{eff} = \hat{H}_0 + \frac{1}{\omega} \sum_{n=1}^{\infty} \frac{1}{n} [\hat{H}_n, \hat{H}_{-n}] + \mathcal{O}\left(\frac{1}{\omega^2}\right), \quad (\text{C1})$$

where

$$\hat{H}_n = \frac{1}{T} \int_0^T dt e^{-in\omega t} \hat{H}(t), \quad (\text{C2})$$

denotes the Fourier components of $\hat{H}(t)$ (with $n = 0, 1, 2, \dots$). For the particular case of the many-body Hamiltonian Eq. (B1), the fermionic anti-commutation relation gives

$$\hat{H}_{eff} = \sum_{\mathbf{k}} \hat{\psi}_{\mathbf{k}}^\dagger \hat{h}_{eff}(\mathbf{k}) \hat{\psi}_{\mathbf{k}}, \quad (\text{C3})$$

with

$$\hat{h}_{eff}(\mathbf{k}) = \hat{h}_0(\mathbf{k}) + \hat{m}(\mathbf{k}), \quad (\text{C4})$$

$$\hat{m}(\mathbf{k}) = \frac{1}{\omega} \sum_{n=1}^{\infty} \frac{1}{n} [\hat{h}_n(\mathbf{k}), \hat{h}_{-n}(\mathbf{k})], \quad (\text{C5})$$

as defined in the main text. Note that $\hat{h}_n(\mathbf{k})$ has the same form of the first-quantized Hamiltonian in Eq. (B2) (or Eq. (B7), or Eq. (B9) depending on which phase of Cd_3As_2 we are considering), but the functions preceding the Pauli matrices are replaced by their Fourier component after minimal coupling. For instance, $M(\mathbf{k}) \rightarrow M_n(\mathbf{k}) = (1/T) \int_0^T e^{-in\omega t} M(\mathbf{k} + \mathbf{A}(t))$. Note that $\hat{h}_0(\mathbf{k})$ is the time-average of the time-dependent first-quantized Hamiltonian $\hat{h}(\mathbf{k} + \mathbf{A}(t))$.

The term proportional to $1/\omega$ in $\hat{h}_{eff}(\mathbf{k})$ [Eq. (C5)], acts as a mass term in the location of the Dirac nodes of the unperturbed band structure and, therefore, we call it *light-induced mass term*. It has nine distinct contributions as a result of the commutations of the Pauli matrices:

$$\begin{aligned} \hat{m}(\mathbf{k}) = & m_{1,\mathbf{k}} \sigma_z \tau_y + m_{2,\mathbf{k}} \sigma_0 \tau_x + m_{3,\mathbf{k}} \sigma_z \tau_z + m_{4,\mathbf{k}} \sigma_x \tau_y + m_{5,\mathbf{k}} \sigma_y \tau_0 \\ & + m_{6,\mathbf{k}} \sigma_x \tau_z + m_{7,\mathbf{k}} \sigma_y \tau_y + m_{8,\mathbf{k}} \sigma_x \tau_0 + m_{9,\mathbf{k}} \sigma_y \tau_z. \end{aligned} \quad (\text{C6})$$

$m_{3,\mathbf{k}}$, $m_{4,\mathbf{k}}$ and $m_{9,\mathbf{k}}$ are always present (both semimetallic and insulating phases) and are given by

$$m_{1,\mathbf{k}} = \frac{2i}{\omega} \sum_{n=1}^{\infty} \frac{1}{n} (M_{n,\mathbf{k}} P_{-n,\mathbf{k}} - M_{-n,\mathbf{k}} P_{n,\mathbf{k}}), \quad (\text{C7})$$

$$m_{2,\mathbf{k}} = \frac{2i}{\omega} \sum_{n=1}^{\infty} \frac{1}{n} (M_{n,\mathbf{k}} Q_{-n,\mathbf{k}} - M_{-n,\mathbf{k}} Q_{n,\mathbf{k}}), \quad (\text{C8})$$

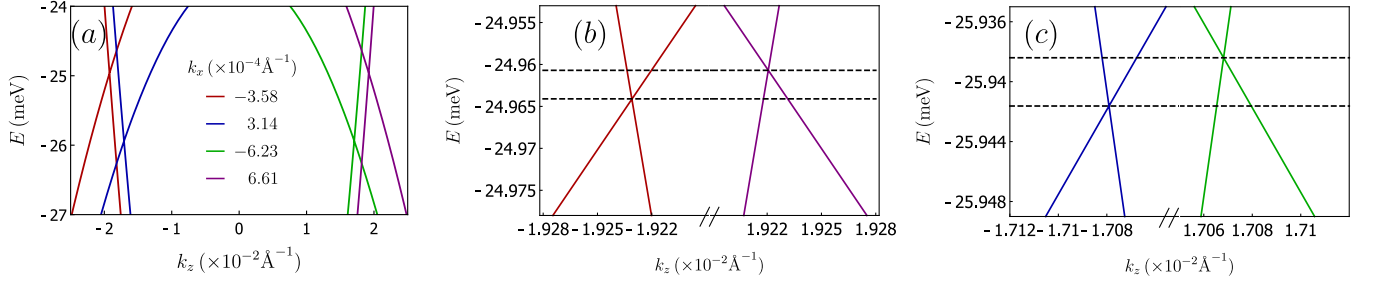


FIG. 3. (a) Cuts with $k_x = k_y$ of the bulk bands of Cd_3As_2 irradiated with BCL. We set the incidence direction normal to (112) surface, $\omega = 300 \text{ meV}$, $\mathcal{A}_0 = 2.6 \times 10^{-2} \text{ \AA}^{-1}$ and $\alpha = \pi/2$. Panels (b) and (c) are zooms of panels (a) to highlight the energy separation of the cones.

$$m_{3,\mathbf{k}} = -\frac{2i}{\omega} \sum_{n=1}^{\infty} \frac{1}{n} (P_{n,\mathbf{k}} Q_{-n,\mathbf{k}} - P_{-n,\mathbf{k}} Q_{n,\mathbf{k}}) . \quad (\text{C9})$$

On the other hand, $m_{4,\mathbf{k}}$, $m_{5,\mathbf{k}}$ and $m_{6,\mathbf{k}}$ only exist in strained Cd_3As_2 with B_{1g} -type strain. They take the forms

$$m_{4,\mathbf{k}} = \frac{2i}{\omega} \sum_{n=1}^{\infty} \frac{1}{n} (M_{n,\mathbf{k}} B_{-n,\mathbf{k}} - M_{-n,\mathbf{k}} B_{n,\mathbf{k}}) , \quad (\text{C10})$$

$$m_{5,\mathbf{k}} = -\frac{2i}{\omega} \sum_{n=1}^{\infty} \frac{1}{n} (B_{n,\mathbf{k}} P_{-n,\mathbf{k}} - B_{-n,\mathbf{k}} P_{n,\mathbf{k}}) , \quad (\text{C11})$$

$$m_{6,\mathbf{k}} = -\frac{2i}{\omega} \sum_{n=1}^{\infty} \frac{1}{n} (B_{n,\mathbf{k}} Q_{-n,\mathbf{k}} - B_{-n,\mathbf{k}} Q_{n,\mathbf{k}}) . \quad (\text{C12})$$

Lastly, $m_{7,\mathbf{k}}$, $m_{8,\mathbf{k}}$ and $m_{9,\mathbf{k}}$ are only present if strain of type B_{2g} is applied. They have the same form as $m_{4,\mathbf{k}}$, $-m_{5,\mathbf{k}}$ and $m_{6,\mathbf{k}}$, respectively, but with $M_{n,\mathbf{k}}$, $P_{n,\mathbf{k}}$ and $Q_{n,\mathbf{k}}$ replaced by $\tilde{M}_{n,\mathbf{k}}$, $\tilde{P}_{n,\mathbf{k}}$ and $\tilde{Q}_{n,\mathbf{k}}$.

In general, both $h_0(\mathbf{k})$ and the light-induced mass terms break symmetries of the bare Hamiltonian, but, ultimately, the latter plays a significant role in the topological transitions. That is because only \mathbf{k} is able to lift the two-fold degeneracy of the bulk bands of the bare Hamiltonian. $h_0(\mathbf{k})$ only shifts the position of the original Dirac nodes.

The spectrum of the effective Hamiltonian obtained with a three-fold BCL incident perpendicular to the (112) surface of Cd_3As_2 is shown in Fig. 3 (a). Because of the simultaneous break of inversion and time-reversal symmetries, the Weyl cones are separated in momentum and energy as highlighted in 3 (b) and (c).

Both CL and BCL generate the same combination of Pauli matrices, as shown in see Eq.(C6). The difference between these two types of light is manifested in the momentum-dependence of $m_j(\mathbf{k})$. The functional form of these functions depends on the polarization state and incidence direction of the light. Therefore, the same term can break distinct symmetries in the CL and BCL cases. As an example, $m_{1,\mathbf{k}}$, preserves π rotation around the \hat{z} -axis ($C_{2,z}$) for a single CL, but this symmetry is broken by the same mass-term in the BCL case. In the table III, we contrast the symmetries preserved by each $m_{j,\mathbf{k}}$ generated in the absence of strain by a CL and by a BCL. In this table, both

Mass term	CL	BCL
$m_{1,\mathbf{k}}$	$C_{2z}, \mathcal{I}, M_z, \Theta C_{2x}, \Theta C_{2y}, \Theta M_x, \Theta M_y$	$M_z, \Theta C_{2y}, \Theta M_x$
$m_{2,\mathbf{k}}$	$C_{2z}, \mathcal{I}, M_z, \Theta C_{2x}, \Theta C_{2y}, \Theta M_x, \Theta M_y$	$M_z, \Theta C_{2y}, \Theta M_x$
$m_{3,\mathbf{k}}$	$C_{2z}, C_{2z}, C_{4z}^+, C_{4z}^-, \mathcal{I}, M_z, \mathcal{I} C_{4z}^+, \mathcal{I} C_{4z}^-, \Theta C_{2x}, \Theta C_{2y}, \Theta C_{2,[110]}, \Theta C_{2x,[110]}, \Theta M_x, \Theta M_y, \Theta M_{[110]}, \Theta M_{[1\bar{1}0]}$	$M_z, \Theta C_{2y}, \Theta M_x$

TABLE III. Symmetries of the original D_{4h} point group (plus time-reversal Θ) that is preserved by each of the mass terms induced by a CL incident parallel to \hat{z} and by a BCL with and the same incidence direction and $\alpha = 0$. Here we focus in the semimetallic case, where no strain is applied to the system. Θ refers to TR symmetry and \mathcal{I} to spatial inversion.

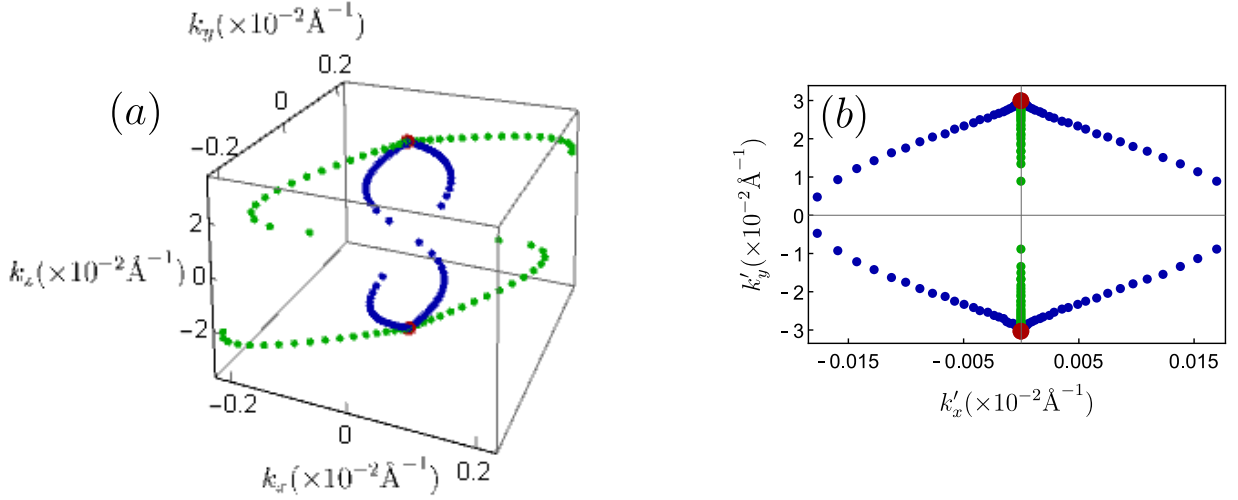


FIG. 4. (a) Evolution of the position of the Weyl nodes, in momentum space, as a function of the light amplitude (\mathcal{A}_0) when Cd_3As_2 is irradiated with (i) a CL light (green points) normal to the (112) surface with $0 \leq \mathcal{A}_0 \leq 3.8 \times 10^{-2} \text{ \AA}^{-1}$ and (ii) BCL (blue points) normal to the (112) surface with $0 \leq \mathcal{A}_0 \leq 2.9 \times 10^{-2} \text{ \AA}^{-1}$ and $\alpha = 0$. In both cases, we set $\omega = 300 \text{ meV}$. Besides, the red points denote the positions of the original Dirac nodes (in the absence of light). Panel (b) shows the projections of the points of panel (a) in the (112) surface

types of light have incidence direction \hat{z} .

Appendix D: Controlling the position of the Weyl nodes

Both the amplitude of the light \mathcal{A}_0 (both BCL and CL) and the relative phase of the BCL α controls the position of the light-induced Weyl nodes. The effect of α is shown in Fig.1 (c) in the main text. Here, to further illustrate the differences between CL and BCL, we show in Fig.4 (a) the trajectory in momentum space of the Weyl nodes induced by a CL (green dots) and BCL (blue dots) as a function of \mathcal{A}_0 . Here, both CL and BCL are incident normal to the (112) surface of Cd_3As_2 and we set $\alpha = 0$. Fig.4 (b) is a projection of Fig.4 (a) in the (112) surface.

Appendix E: Higher-order terms in the effective Hamiltonian

Terms of order $1/\omega^2$ or higher in the effective time-independent Hamiltonian in Eq.(C4) involves nested commutators of $\hat{h}_n(\mathbf{k})$. In particular, the second-order term reads

$$\hat{h}^{(2)}(\mathbf{k}) = \frac{1}{2\omega^2} (s_1(\mathbf{k}) + s_2(\mathbf{k})) , \quad (\text{E1})$$

with

$$s_1(\mathbf{k}) = \sum_{n=1}^{\infty} \frac{1}{n^2} \left(\left[\left[\hat{h}_n, \hat{h}_0 \right], \hat{h}_{-n} \right] + \text{h.c.} \right) , \quad (\text{E2})$$

$$s_2(\mathbf{k}) = \frac{2}{3} \sum_{n,n'=1}^{\infty} \frac{1}{nn'} \left(\left[\hat{h}_n, \left[\hat{h}_{n'}, \hat{h}_{-n-n'} \right] \right] - 2 \left[\hat{h}_n, \left[\hat{h}_{-n'}, \hat{h}_{n'-n} \right] \right] + \text{h.c.} \right) . \quad (\text{E3})$$

Importantly, these nested commutators form a closed group. We already saw that for $\hat{h}_n(\mathbf{k})$ composed by a linear combination of $\sigma_0\tau_z$, $\sigma_x\tau_x$, $\sigma_y\tau_x$, $\sigma_z\tau_x$, $\sigma_0\tau_y$ and $\sigma_0\tau_0$, the commutator of the type $[\hat{h}_n, \hat{h}_m]$ yields the nine possible Kronecker products of Pauli matrices shown in Eq.(C6). The next order commutator $[[\hat{h}_n, \hat{h}_m], \hat{h}_l]$ accompanying terms proportional to $1/\omega^2$ produces exactly the same Pauli matrices in $\hat{h}_n(\mathbf{k})$ and, therefore, only dresses $\hat{h}_0(\mathbf{k})$. This structure repeats for higher-order commutators and we conclude that the corrections of order $\mathcal{O}(1/\omega^\alpha)$, with α ,

even dresses $\hat{h}_0(\mathbf{k})$ and contribute to the shift of the original Dirac nodes (in the semi-metallic phase. For *odd* α , on the other hand, dresses $\hat{m}(\mathbf{k})$ and contribute to the momentum and energy split of the Weyl nodes. These corrections, however, are very small in the limit that $\omega > E_{Lif}$ (Lifshitz energy). Indeed, in the next section we show that the first order perturbation theory in Eqs.(C4) and (C5) reproduces accurately the Floquet quasienergies for the values of light frequencies we used in this manuscript.

Appendix F: Validity of the high-frequency expansion

In Sec.E, we saw that higher-order terms in the high-frequency expansion come with powers of $1/\omega^n$, which becomes very small when $\omega > E_{Lif}$ justifying the truncation of the effective Hamiltonian in first-order in ω . A complementary way to show the validity of this approximation is to calculate the Floquet quasienergies and compare them with the bulk bands of the effective Hamiltonian defined in Eq.(C4).

The Floquet quasienergies the eigenvalues of the Floquet Hamiltonian, which matrices elements are given by [7]

$$(H_F)_{m,n} = \frac{1}{T} \int_0^T dt e^{i(m-n)\omega t} \hat{h}(\mathbf{k} + \mathbf{A}(t)) - m\omega \delta_{m,n} = \hat{h}_{n-m}(\mathbf{k}) - m\omega \delta_{m,n} . \quad (F1)$$

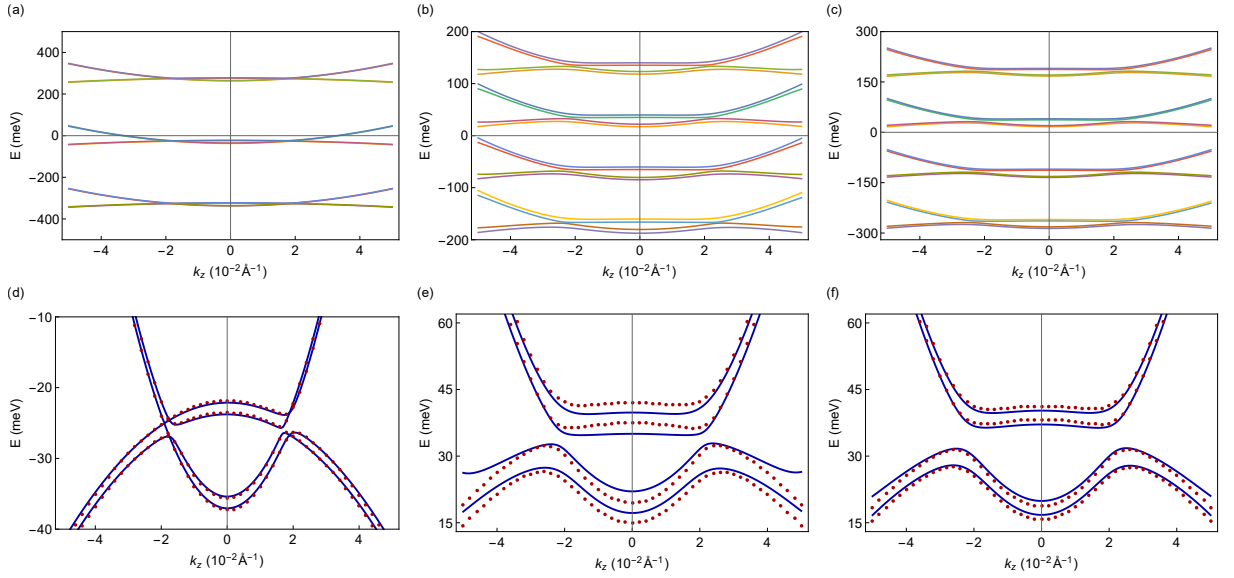


FIG. 5. Floquet quasienergies obtained for the minimal model for Cd_3As_2 irradiated with BCL normal to (112) with frequencies (a) $\omega = 300$ meV, (b) $\omega = 100$ meV and (c) $\omega = 150$ meV. In (b) and (c), BCL is combined with B_{2g} -type strain. Panels (d)-(f) correspond to the quasi-energies of (a)-(c) in the zero-photon sector (solid lines) overlaid to the band dispersion of the effective Hamiltonian obtained through high-frequency expansion (dots). In all panels, the BCL relative phase and amplitude are set to $\alpha = \pi/2$ and $\mathcal{A}_0 = 2.6 \times 10^{-2} \text{Å}^{-1}$, respectively.

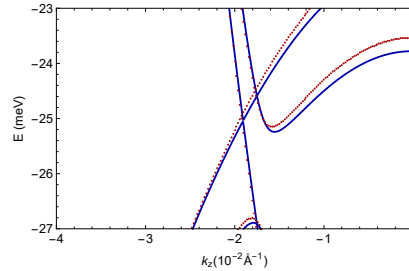


FIG. 6. Zoom of the quasienergies and effective Hamiltonian dispersion around the Weyl cone shown in Fig.6(a).

Here, $\hat{h}(\mathbf{k})$ is the first-quantized Hamiltonian defined in Eq.(B2) (or Eqs.(B7) and (B9) in the presence of strain) and $\hat{h}_n(\mathbf{k})$ represents its Fourier coefficient as defined in Eq.(C2).

Exact diagonalization of the Floquet Hamiltonian for the same values of the light parameters adopted in the main text yields a quasienergy spectrum where the different photon sectors are well separated in energy [see Fig.5 (a)-(c)]. Furthermore, for the range in momentum space where the $k.p$ model for Cd_3As_2 holds, there is no hybridization between different photon sectors as long as $\omega > E_{Lif}$, as expected.

Figs.5 (d)-(f) are zooms of Figs.5 (a)-(c), respectively, in the zero-photon sector. In each panel, the eigenvalues effective Hamiltonian defined in Eq.(C4) (dots) are overlaid to the quasienergies (solid lines). We obtain an excellent agreement between them for $\omega > E_{Lif}$, as shown in Figs.5(d). A zoom around the Weyl node in 5(d) shows only a small quantitative difference, of order of 10^{-4}\AA^{-1} in the position of the node obtained through exact diagonalization in comparison with the high-frequency expansion [see Fig.6].

As the light frequency becomes comparable with the Lifshitz energy, however, quantitative differences emerges. This can be seen in Fig.5, where $\omega = 100\text{ meV}$ and $E_{Lif} = 80\text{ meV}$. Even in this case, the frequency is still larger enough such that hybridization of quasienergies in different Floquet sectors are absent around the center of the Brillouin zone.

Fig.5 (a) and (d) was obtained using the same parameters as in Fig.1 (b) of the main text. The remaining panels were obtained with the parameters used in Fig.4 of the main text with $\omega = 100\text{ meV}$ (b) and (e) and $\omega = 150\text{ meV}$ in (c) and (f). We checked that an excellent agreement between exact diagonalization of the Floquet Hamiltonian and high-frequency expansion up to $\mathcal{O}(1/\omega)$ holds for all choices of parameters in the main text.

Appendix G: Surface states

Here, we detail the method we used to calculate the surface states (SS) shown in the main text. In the following, we define two coordinate systems: (x, y, z) denotes the material frame of reference, where the \hat{x} , \hat{y} and \hat{z} are parallel to the crystallographic axes [100], [010] and [001], respectively. Since we are dealing with a tetragonal crystal, \hat{k}_x , \hat{k}_y and \hat{k}_z are also aligned with [100], [010] and [001]. The laboratory frame of reference, on the other hand, is given by (x', y', z') . The momentum components in the laboratory frame are k'_x , k'_y , and k'_z . As we will shortly see, (x, y, z) and (x', y', z') are related by a unitary transformation that depends on which material surface we want to probe for SS.

We calculate the SS by searching for evanescent states at the $z' = 0$ termination of a semi-infinite slab of Cd_3As_2 defined in the $z' < 0$ region. Instead of writing a tight-binding model with open boundaries along z' (x' and y') and solving for the surface states, here, we calculate them directly from the $k.p$ model. We use an approach similar to Ref. [4]. Evanescent states at $z' = 0$ have to fulfill two conditions: (i) $\psi_{\mathbf{k}'}(z' = 0) = 0$ and (ii) $\psi_{\mathbf{k}'}(z' \rightarrow -\infty) = 0$, where $\psi_{\mathbf{k}'}(\mathbf{r}') = u_{\mathbf{k}'}(\mathbf{r}')e^{i\mathbf{k}' \cdot \mathbf{r}'}$ are the Bloch wave-functions and $u_{\mathbf{k}'}(\mathbf{r}')$ are eigenstates of the first-quantized Hamiltonian $\hat{h}(\hat{U}_{(hkl)}^{-1}\mathbf{k}')$. Here, $\hat{h}(\mathbf{k})$ refer to either the bare first-quantized Hamiltonian [Eq. (B2), Eq. (B7) or Eq. (B9)] if light is absent, or to the effective first-quantized Floquet Hamiltonian [Eq. (C4)] if light is taken into account. The matrix $\hat{U}_{(hkl)}$ is the unitary transformation that aligns the normal to crystal surface labeled by the Miller indices (hkl) with \hat{z}' . As an example, let's say that we want to calculate the SS at the (112) surface. The normal to such surface points at the direction $[1, 1, \frac{1}{2}] = a(\hat{x} + \hat{y}) + \frac{c}{2}\hat{z} = a(\hat{x} + \hat{y} + \hat{z})$, and therefore, $\hat{z}' = (\hat{x} + \hat{y} + \hat{z})/\sqrt{3}$. Besides, the two orthogonal direction in the (112), $[1\bar{1}0] = a(\hat{x} - \hat{y})$ and $[11\bar{1}] = a(\hat{x} + \hat{y} - 2\hat{z})$, determine the x' and y' axes. This give us the transformation relation between laboratory and material frames of reference, $\mathbf{r}' = \hat{U}_{(112)}\mathbf{r}$ (and, equivalently $\mathbf{k}' = \hat{U}_{(112)}\mathbf{k}$), where

$$\hat{U}_{(112)} = \begin{pmatrix} 1/\sqrt{2} & -1/\sqrt{2} & 0 \\ 1/\sqrt{6} & 1/\sqrt{6} & -2/\sqrt{6} \\ 1/\sqrt{3} & 1/\sqrt{3} & 1/\sqrt{3} \end{pmatrix}. \quad (\text{G1})$$

Similarly, for the $(1\bar{1}0)$ considered in the main text,

$$\hat{U}_{(1\bar{1}0)} \equiv \begin{pmatrix} 1/\sqrt{2} & 1/\sqrt{2} & 0 \\ 0 & 0 & 1 \\ 1/\sqrt{2} & -1/\sqrt{2} & 0 \end{pmatrix}. \quad (\text{G2})$$

Condition (ii) above is satisfied for complex k'_z with a negative imaginary part $\kappa < 0$. For each point in the surface Brillouin Zone (k'_x, k'_y) and for a fixed energy E , we look for the set of complex k'_z that are solutions of the

characteristic polynomial

$$\det(\hat{h}(\hat{U}_{hkl}^{-1}\mathbf{k}') - E\mathbf{1}) = 0, \quad (\text{G3})$$

and select only those with $\kappa < 0$. Besides, only solutions with κ that differ by more than a numerical precision of 10^{-5} are chosen. Not all of these complex k'_z solutions gives rise to true eigenstates of the Hamiltonian. Therefore, we substitute each of the solutions back in $\hat{h}(\hat{U}_{hkl}^{-1}\mathbf{k}')$ calculate its eigenvalues and eigenvectors. The eigenvectors whose eigenvalue matches the initial energy cut E correspond to localized states that decay exponentially in the region $z' < 0$. To obtain the SS, the condition $\psi_{\mathbf{k}'}(z' = 0) = 0$ still needs to be fulfilled, and this is done by linear combinations of the eigenvectors just collected, which we hereafter denote by

$$\{|u_{\mathbf{k}'_1}\rangle, |u_{\mathbf{k}'_2}\rangle, \dots\}. \quad (\text{G4})$$

Note that since the coefficients of Eq. (G3) are real, its solution comes in complex conjugated pairs. Therefore, the maximum number of vectors in the set (G4) is half of the order of Eq. (G3).

A linear combination of the Bloch wave-functions, at $z' = 0$, constructed with the elements of Eq. (G4)

$$\phi(z' = 0) = \sum_i \alpha_i u_{\mathbf{k}',i}(0), \quad (\text{G5})$$

fulfills the condition $\phi(z' = 0) = 0$ if the determinant of the matrix M whose columns are the $|u_{\mathbf{k}'_i}\rangle$ entering in Eq. (G5) is zero. In this case, a SS with energy E exists at (k'_x, k'_y) . Small deviations from zero means that the surface state does not exactly vanish at $z' = 0$, but its amplitude is small. We accept results states with $|\det M| \leq 5 \times 10^{-3}$. This analysis is applied to all points a the grid $-0.05 \text{\AA}^{-1} \leq k'_x, k'_y \leq 0.05 \text{\AA}^{-1}$, where the $k.p$ model is valid and these points are colored according to the value of $\det(M)$.

Importantly, since $|u_{\mathbf{k}'_i}\rangle$ is 4-dimensional, we need, at least, four different states in Eq. (G4) to be able to get

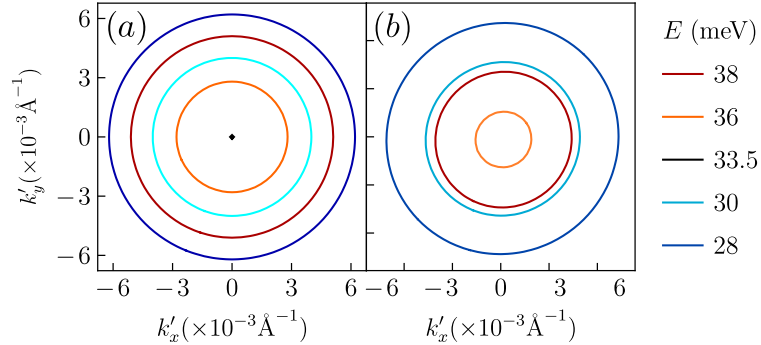


FIG. 7. Energy cuts of the surface states of strained Cd_3As_2 in the (001) surface (a) in the absence of light and (b) in the presence of a CL incident normal to (112). We set the strain type to be B_{1g} , $\omega = 400$ meV and $\mathcal{A}_r = 2.4 \times 10^{-2} \text{\AA}^{-1}$.

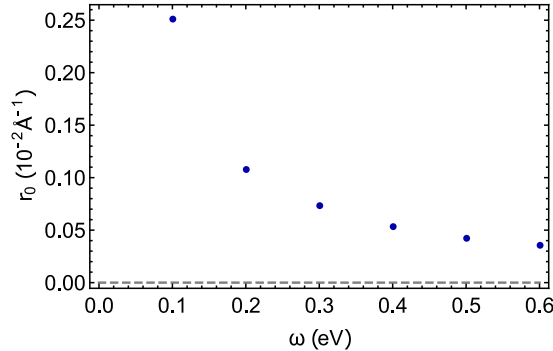


FIG. 8. Position $r_0 = \sqrt{k_x'^2 + k_y'^2}$ of the surface Dirac node in the (110) surface as a function of BCL frequency. We set the incidence direction to be normal to (112) and $\mathcal{A}_0 = 2.6 \times 10^{-2} \text{\AA}^{-1}$ and $\alpha = \pi/2$.

$\phi(z' = 0) = 0$. This implies that, in the absence of light, since all the bands are two-fold degenerate, a minimum of two complex k'_z with $\kappa < 0$ needs to be found in Eq. (G3). When the light field is included, on the other hand, the degeneracy of the bands is lifted (except at the Weyl nodes) and the minimum number of distinct solutions increases to four.

We applied this technique for semimetallic and the insulating phases of Cd_3As_2 . Fig.7 shows cuts of the surface states in Fig.3 of the main text. Fig.8, shows the position of the node of the surface Dirac cone in (110) surface as a function of the frequency of the BCL. In the latter figure, the parameters are set to be the same as in Fig.4 in the main text.

Appendix H: Temperature dependence of the GME effect

The gyromagnetic effect (GME) describes the current density \mathbf{J} that is induced in a system in response of an slowly-oscillating external magnetic field. This is not an equilibrium current, but rather a low-frequency response of a system that vanishes in insulators and is directly proportional to the energy separation of the Weyl nodes of a non-centrosymmetric Weyl semimetal. In this section, we derive the temperature dependence of the GME effect in Weyl semimetal where the Weyl nodes are separated both in energy and momentum.

The GME effect is fundamentally different from the chiral magnetic effect (CME) although the form of the induced currents in both effects have similar forms. In contrast to the CME, GME is not governed by a geometric property of the bulk bands. It is the low-frequency limit of natural gyrotropy in non-centrosymmetric metals and is governed by the magnetic moment of the Bloch states at the Fermi level [11, 12],

$$\mathbf{J}_i = \alpha_{ij}^{GME} B_j, \quad (\text{H1})$$

$$\alpha_{ij}^{GME} = \frac{i\Omega\tau}{1 - i\Omega\tau} \sum_{n \in \text{occ}} \int d\mathbf{k} \frac{\partial f_{n,\mathbf{k}}}{\partial \varepsilon_{n,\mathbf{k}}} v_{n,\mathbf{k}}^{(i)} m_{n,\mathbf{k}}^{(j)}. \quad (\text{H2})$$

Here, $i, j = x, y, z$ denotes Cartesian components, Ω corresponds to the frequency of the magnetic field and τ^{-1} is the electron scattering rate due to disorder. Besides, $f_{n,\mathbf{k}} = (\exp(\varepsilon_{n,\mathbf{k}} - \mu) + 1)^{-1}$ is the Fermi-Dirac distribution function. $\varepsilon_{n,\mathbf{k}}$ denotes the dispersion of the Bloch bands, whose occupation is controlled by the chemical potential μ . Note that the sum over the band index n runs over the occupied bands only. The other two quantities appearing in the integrand of the GME tensor in Eq.H2 are the band velocity $\mathbf{v}_{n,\mathbf{k}} = (\partial_{\mathbf{k}} \varepsilon_{n,\mathbf{k}})/\hbar$, with $\partial_{\mathbf{k}} \equiv \partial/\partial \mathbf{k}$, and the magnetic moment of a Bloch electron,

$$\mathbf{m}_{n,\mathbf{k}} = \frac{e}{2\hbar} \text{Im} \left\langle \partial_{\mathbf{k}} u_{n,\mathbf{k}} \left| \times \left[\hat{h}(\mathbf{k}) - \varepsilon_{n,\mathbf{k}} \right] \right| \partial_{\mathbf{k}} u_{n,\mathbf{k}} \right\rangle. \quad (\text{H3})$$

In the expression above, $|u_{n,\mathbf{k}}\rangle$ is the periodic part of the Bloch wave-function, which is the eigenstate of the first-quantized Hamiltonian, $\hat{h}(\mathbf{k}) |u_{n,\mathbf{k}}\rangle = \varepsilon_{n,\mathbf{k}} |u_{n,\mathbf{k}}\rangle$. The expectation value of the spin of the Bloch state also contributes to the the magnetic moment in Eq.(H3) [11], but here, following the approach in Ref. 11 we focus only on its orbital part.

The form of the GME tensor in Eq.(H2) was obtained through the *uniform limit* of the linear order tensor, $\alpha^{GME} = \lim_{\Omega \rightarrow 0} \lim_{q \rightarrow 0} \alpha(\mathbf{q}, \omega)$. Here, the $\Omega \rightarrow 0$ limit means that $\hbar\Omega \ll \epsilon_{inter}$, where ϵ_{inter} is the energy scale associated with interband transitions. For the parameters of Fig.1(a) in the main text, this gives an upper limit of order of GHz for Ω . As we can see from the prefactor in the right-hand side of Eq.(H2), the GME effect is suppressed by disorder and requires $\Omega\tau \gg 1$, which gives a lower bound for Ω .

The expression in Eq.(H2) gets greatly simplified in the case of Weyl semimetal. In the vicinity of a Weyl node, $\varepsilon_{n,\mathbf{k}} = \varepsilon_0 - \hbar n v_F k$ and $\mathbf{m}_{n,\mathbf{k}} = -e v_F \chi \mathbf{k} / (2k^2)$, where v_F is the Fermi velocity, χ is the node chirality and $n = \pm 1$. Therefore, for a Fermi surface with pockets coming from two Weyl cones, one with node slightly above the Fermi level and the other slightly below, the GME tensor at $T = 0$ takes the well-known form [11]

$$\alpha_{ij}^{(GME)} = \delta_{i,j} \frac{e^2}{3\hbar^2} \Delta E, \quad (\text{H4})$$

where ΔE is the energy separation between the the Weyl nodes.

Interestingly, because of the linear dispersion of the Weyl nodes, Eq.(H4) is robust to thermal effects. At finite

temperatures, Eq.(H2) becomes $\alpha_{i,j}^{(GME)} = \delta_{i,j} e^2 (\chi_1 R_1 + \chi_2 R_2) / (3h^2)$, where

$$R_j \equiv \frac{1}{T} \int_{-\infty}^{\infty} d\varepsilon \frac{(\varepsilon_{0,j} - \varepsilon)}{4 \cosh^2(\frac{\varepsilon - \mu}{2T})} = \varepsilon_{0,j} - \mu, \quad (\text{H5})$$

recovering the same expression as in the zero temperature case. This effect will be suppressed when the band dispersion deviates from linear and when a finite bandwidth is taken into account.

-
- [1] J. W. Edington, Electron diffraction in the electron microscope, in *Electron Diffraction in the Electron Microscope* (Springer, 1975) pp. 1–77.
 - [2] M. N. Ali, Q. Gibson, S. Jeon, B. B. Zhou, A. Yazdani, and R. J. Cava, The crystal and electronic structures of Cd₃As₂, the three-dimensional electronic analogue of graphene, *Inorganic chemistry* **53**, 4062 (2014).
 - [3] Z. Wang, H. Weng, Q. Wu, X. Dai, and Z. Fang, Three-dimensional Dirac semimetal and quantum transport in Cd₃As₂, *Phys. Rev. B* **88**, 125427 (2013).
 - [4] P. Villar Arribi, J.-X. Zhu, T. Schumann, S. Stemmer, A. A. Burkov, and O. Heinonen, Topological surface states in strained Dirac semimetal thin films, *Phys. Rev. B* **102**, 155141 (2020).
 - [5] S. Jeon, B. B. Zhou, A. Gyenis, B. E. Feldman, I. Kimchi, A. C. Potter, Q. D. Gibson, R. J. Cava, A. Vishwanath, and A. Yazdani, Landau quantization and quasiparticle interference in the three-dimensional Dirac semimetal Cd₃As₂, *Nature materials* **13**, 851 (2014).
 - [6] D. Varjas, T. Ö. Rosdahl, and A. R. Akhmerov, Qsymm: Algorithmic symmetry finding and symmetric hamiltonian generation, *New Journal of Physics* **20**, 093026 (2018).
 - [7] T. Mikami, S. Kitamura, K. Yasuda, N. Tsuji, T. Oka, and H. Aoki, Brillouin-Wigner theory for high-frequency expansion in periodically driven systems: Application to Floquet topological insulators, *Phys. Rev. B* **93**, 144307 (2016).
 - [8] S. Rahav, I. Gilary, and S. Fishman, Effective Hamiltonians for periodically driven systems, *Phys. Rev. A* **68**, 013820 (2003).
 - [9] A. Eckardt and E. Anisimovas, High-frequency approximation for periodically driven quantum systems from a floquet-space perspective, *New journal of physics* **17**, 093039 (2015).
 - [10] M. Bukov, L. D'Alessio, and A. Polkovnikov, Universal high-frequency behavior of periodically driven systems: from dynamical stabilization to floquet engineering, *Advances in Physics* **64**, 139 (2015).
 - [11] S. Zhong, J. E. Moore, and I. Souza, Gyrotropic Magnetic Effect and the Magnetic Moment on the Fermi Surface, *Phys. Rev. Lett.* **116**, 077201 (2016).
 - [12] J. Ma and D. A. Pesin, Chiral Magnetic Effect and Natural Optical Activity in Metals with or without Weyl Points, *Phys. Rev. B* **92**, 235205 (2015).